The Genetic Architecture of Multimodal Human Brain Age

Junhao Wen[1*], Bingxin Zhao[2], Zhijian Yang[3], Guray Erus[3], Ioanna Skampardoni[3], Elizabeth Mamourian[3], Yuhan Cui[3], Gyujoon Hwang[3], Jingxuan Bao[4], Aleix Boquet-Pujadas[5], Zhen Zhou[3], Yogasudha Veturi[6], Marylyn D. Ritchie[7], Haochang Shou[3], Paul M. Thompson[8], Li Shen[4], Arthur W. Toga[9], Christos Davatzikos[3]

[1]Laboratory of AI and Biomedical Science (LABS), Stevens Neuroimaging and Informatics Institute, Keck School of Medicine of USC, University of Southern California, Los Angeles, California, USA
[2]Department of Statistics and Data Science, University of Pennsylvania, Philadelphia, PA, USA
[3]Artificial Intelligence in Biomedical Imaging Laboratory (AIBIL), Center for AI and Data Science for Integrated Diagnostics (AI^{2}D), Perelman School of Medicine, University of Pennsylvania, Philadelphia, USA
[4]Department of Biostatistics, Epidemiology and Informatics, University of Pennsylvania Perelman School of Medicine, Philadelphia, USA
[5]Biomedical Imaging Group, EPFL, Lausanne, Switzerland
[6]Department of Biobehavioral Health and Statistics, Penn State University, University Park, PA, USA
[7]Department of Genetics and Institute for Biomedical Informatics, Perelman School of Medicine, University of Pennsylvania, Philadelphia, PA, USA
[8]Imaging Genetics Center, Mark and Mary Stevens Neuroimaging and Informatics Institute, Keck School of Medicine of USC, University of Southern California, Marina del Rey, California
[9]Laboratory of Neuro Imaging (LONI), Stevens Neuroimaging and Informatics Institute, Keck School of Medicine of USC, University of Southern California, Los Angeles, California, USA

[*]Corresponding author:
Junhao Wen, junhaowe@usc.edu
2025 Zonal Ave, Los Angeles, CA 90033, United States

Word counts: 4514 words

Abstract

The complex biological mechanisms underlying human brain aging remain incompletely understood, involving multiple body organs and chronic diseases. In this study, we used multimodal magnetic resonance imaging and artificial intelligence to examine the genetic architecture of the brain age gap (BAG) derived from gray matter volume (GM-BAG, *N*=31,557 European ancestry), white matter microstructure (WM-BAG, *N*=31,674), and functional connectivity (FC-BAG, *N*=32,017). We identified sixteen genomic loci that reached genome-wide significance (P-value<$5x10^{-8}$). A gene-drug-disease network highlighted genes linked to GM-BAG for treating neurodegenerative and neuropsychiatric disorders and WM-BAG genes for cancer therapy. GM-BAG showed the highest heritability enrichment for genetic variants in conserved regions, whereas WM-BAG exhibited the highest heritability enrichment in the 5' untranslated regions; oligodendrocytes and astrocytes, but not neurons, showed significant heritability enrichment in WM and FC-BAG, respectively. Mendelian randomization identified potential causal effects of several exposure variables on brain aging, such as type 2 diabetes on GM-BAG (odds ratio=1.05 [1.01, 1.09], P-value=$1.96x10^{-2}$) and AD on WM-BAG (odds ratio=1.04 [1.02, 1.05], P-value=$7.18x10^{-5}$). Overall, our results provide valuable insights into the genetics of human brain aging, with clinical implications for potential lifestyle and therapeutic interventions. All results are publicly available at the MEDICINE knowledge portal: https://labs.loni.usc.edu/medicine.

Main

The advent of artificial intelligence (AI) has provided novel approaches to investigate various aspects of human brain health[1,2], such as normal brain aging[3], neurodegenerative disorders such as Alzheimer's disease (AD)[4], and brain cancer[5]. Based on magnetic resonance imaging (MRI), AI-derived measures of the human brain age[6–8] have emerged as a valuable biomarker for evaluating brain health. More precisely, the difference between an individual's AI-predicted brain age and chronological age – brain age gap (BAG) – provides a means of quantifying an individual's brain health by measuring deviation from the normative aging trajectory. BAG has demonstrated sensitivity to several common brain diseases, clinical variables, and cognitive functions[9], presenting the promising potential for its use in the general population to capture relevant pathological processes.

Brain imaging genomics[10], an emerging scientific field advanced by both computational statistics and AI, uses imaging-derived phenotypes (IDP[11]) from MRI and genetics to offer mechanistic insights into healthy and pathological aging of the human brain. Recent large-scale genome-wide association studies (GWAS)[11–18] have identified a diverse set of genomic loci linked to gray matter (GM)-IDP from T1-weighted MRI, white matter (WM)-IDP from diffusion MRI [fractional anisotropy (FA), mean diffusivity (MD), neurite density index (NDI), and orientation dispersion index (ODI)], and functional connectivity (FC)-IDP from functional MRI. While previous GWAS[19] have associated BAG with common genetic variants [e.g., single nucleotide polymorphism (SNP)], they primarily focused on GM-BAG[9,20–22] or did not comprehensively capture the genetic architecture of the multimodal BAG[19] via post-GWAS analyses in order to biologically validate the GWAS signals. It is crucial to holistically identify the genetic factors associated with multimodal BAGs (GM, WM, and FC-BAG), where each

72 BAG reflects distinct and/or similar neurobiological facets of human brain aging. Furthermore,
73 dissecting the genetic architecture of human brain aging may determine the causal implications,
74 which is essential for developing gene-inspired therapeutic interventions. Finally, numerous risk
75 or protective lifestyle factors and neurobiological processes may also exert independent,
76 synergistic, antagonistic, sequential, or differential influences on human brain health. Therefore,
77 a holistic investigation of multimodal BAGs is urgent to fully capture the genetics of human
78 brain aging, including the genetic correlation, gene-drug disease network, and potential causality.
79 In this study, we postulate that AI-derived GM, WM, and FC-BAG can serve as robust,
80 complementary endophenotypes[23] – close to the underlying etiology – for precise quantification
81 of human brain health.

82 The present study sought to uncover the genetic architecture of multimodal BAG and
83 explore the causal relationships between protective/risk factors and decelerated/accelerated brain
84 age. To accomplish this, we analyzed multimodal brain MRI scans from 42,089 participants from
85 the UK Biobank (UKBB) study[24] and used 119 GM-IDP, 48 FA WM-IDP, and 210 FC-IDP to
86 derive GM, WM, and FC-BAG, respectively. Refer to **Method 1** for selecting the final feature
87 sets for each BAG. We first compared the age prediction performance of different machine
88 learning models using these IDPs. We then performed GWAS to identify genomic loci
89 associated with GM, WM, and FC-BAG in the European ancestry population. In post-GWAS
90 analyses, we constructed a gene-drug-disease network, estimated the genetic correlation with
91 several brain disorders, assessed their heritability enrichment in various functional categories or
92 specific cell types, and calculated the polygenic risk scores (PRS) of the three BAGs. Finally, we
93 performed Mendelian Randomization (MR)[25] to infer the causal effects of several clinical traits
94 and diseases on the three BAGs.

Results

In the first section, we objectively compared the age prediction performance of four machine learning methods using these GM, WM, and FC-IDPs (**Fig. 1A**). To this end, we employed a nested cross-validation (CV) procedure in the training/validation/test dataset (*N*=4000); an independent test dataset (*N*=38,089)[26,27] was held out – unseen until we finalized the models using only the training/validation/test dataset (**Method 1**). The four machine learning models included support vector regression (SVR), LASSO regression, multilayer perceptron (MLP), and a five-layer neural network (i.e., three linear layers and one rectified linear unit layer; hereafter, NN)[28] (**Method 3**). The second section focused on the main GWASs using the European ancestry population (31,557<*N*<32,017) and their sensitivity checks in six scenarios (**Method 4A**). In the last section, we validated the GWAS findings in several post-GWAS analyses, including genetic correlation, gene-drug-disease network, partitioned heritability, PRS calculation, and Mendelian randomization (**Method 4**).

GM, WM, and FC-BAG derived from three MRI modalities

Several findings were observed based on the results from the independent test dataset (*N*=38,089, **Method 1**). First, GM-IDP (4.39<mean absolute error (MAE)<5.35; 0.64<*r*<0.66), WM-IDP (4.92<MAE<7.95; 0.42<*r*<0.65), and FC-IDP (5.48<MAE<6.05; 0.43 <*r*<0.46) achieved gradually a higher MAE and smaller Pearson's correlation (*r*) (**Fig. 1B**, **C**, and **D**). Second, LASSO regression obtained the lowest MAE for GM, WM, and FC-IDP; linear models obtained a lower MAE than non-linear networks (**Fig. 1B**). Third, all models generalized well from the training/validation/test dataset (*N*=4000, **Method 1**) to the independent test dataset. However, simultaneously incorporating WM-IDP from FA, MD, NDI, and ODI resulted in severely

118 overfitting models (**Supplementary eTable 1A**). The observed overfitting may be attributed to
119 many parameters (*N*=38,364) in the network or strong correlations among the diffusion metrics
120 (i.e., FA, MD, ODI, and NDI). Fourth, the experiments stratified by sex did not exhibit
121 substantial differences, except for a stronger overfitting tendency observed in females compared
122 to males using WM-IDP incorporating the four diffusion metrics (**Supplementary eTable 1B**).
123 Detailed results of the CV procedure, including the training, validation, test performance, and
124 sex-stratified experiments, are presented in **Supplementary eTable 1**. In all subsequent genetic
125 analyses, we reported the results using BAG derived from the three LASSO models with the
126 lowest MAE in each modality (**Fig. 1A**), with the "age bias" corrected as in De Lange et al.[29].
127 In the literature, other studies[30–33] have thoroughly evaluated age prediction performance
128 using different machine learning models and input features. More et al.[34] systematically
129 compared the performance of age prediction of 128 workflows (MAE between 5.23–8.98 years)
130 and showed that voxel-wise feature representation (MAE approximates 5-6 years) outperformed
131 parcel-based features (MAE approximates 6-9 years) using conventional machine learning
132 algorithms (e.g., LASSO regression). Using deep neural networks, Peng et al.[30] and Leonardsen
133 et al.[31] reported a lower MAE (nearly 2.5 years) with voxel-wise imaging scans. However, we
134 previously showed that a moderately fitting convolutional neural network (CNN) obtained
135 significantly higher differentiation (a larger effect size) than a tightly fitting CNN (a lower MAE)
136 between the disease and health groups[35]. To summarize, our study's brain age prediction
137 performance aligns with those reported in the existing literature, considering the utilization of
138 low-dimensional hand-crafted IDPs and conventional machine learning algorithms[34].
139 Finally, we calculated the phenotypic correlation (p_c) between GM, WM, and FC-BAG
140 using Pearson's correlation coefficient. GM-BAG and WM-BAG showed the highest positive

correlation (p_c=0.38; P-value<1x10^{-10}; N=30,733); GM-BAG (p_c=0.09; P-value<1x10^{-10}; N=30,660) and WM-BAG (p_c=0.10; P-value<1x10^{-10}; N=31,574) showed weak correlations with FC-BAG (**Fig. 1E**).

Figure 1: **Brain age prediction using three MRI modalities and four machine learning models**

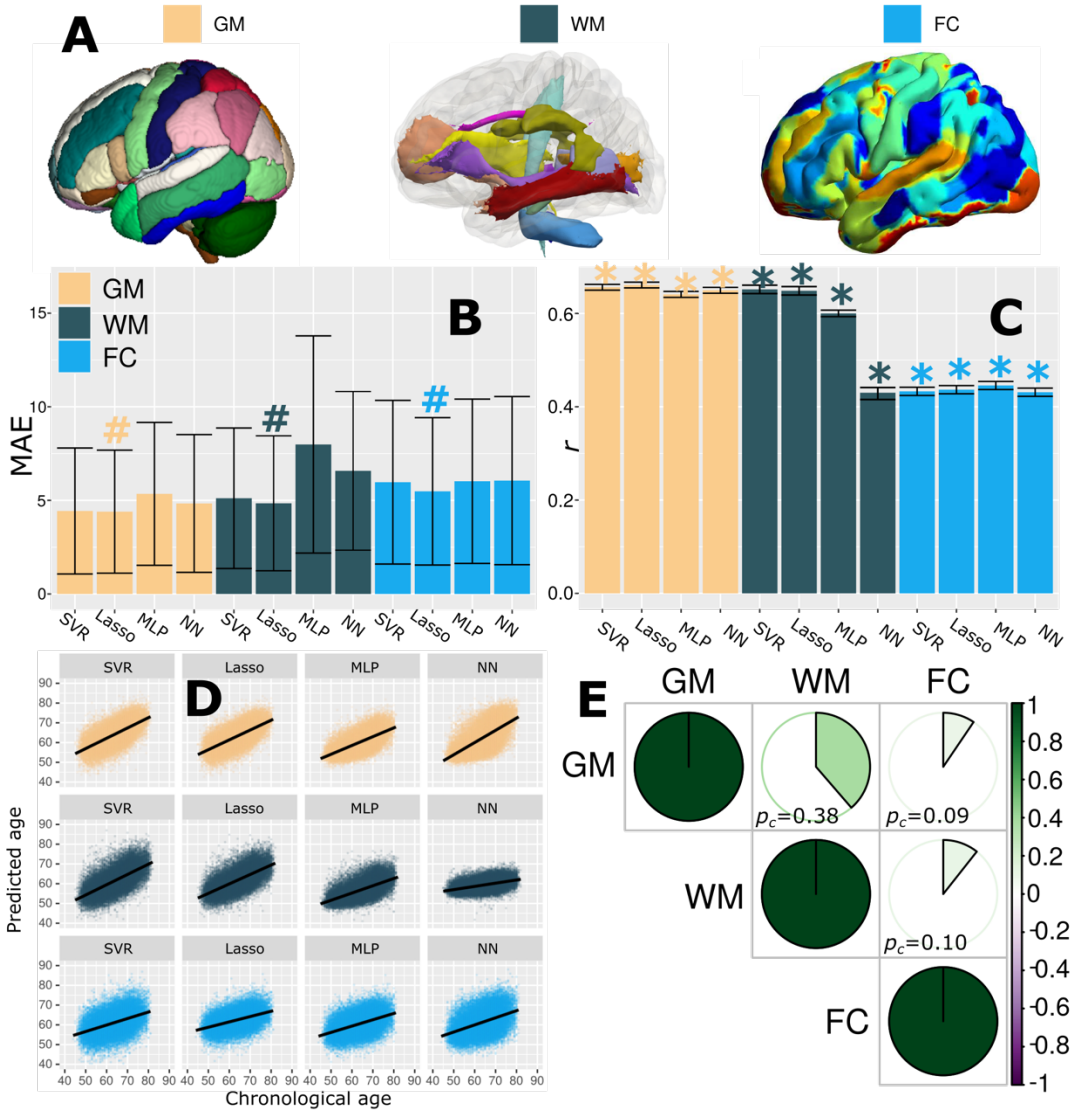

A) Multimodal brain MRI data were used to derive imaging-derived phenotypes (IDP) for T1-weighted MRI (119 GM-IDP), diffusion MRI (48 WM-IDP), and resting-state functional MRI (210 FC-IDP). IDPs for each modality are shown here using different colors based on predefined brain atlases or ICA for FC-IDP. **B**) Linear models achieved lower mean absolute errors (MAE) than non-linear models using support vector regression (SVR), LASSO regression, multilayer perceptron (MLP), and a five-layer neural network (NN). The MAE for the independent test dataset is presented, and the # symbol indicates the model with the lowest MAE for each modality. Error bars represent standard deviation (SD). **C**) Pearson's correlation (*r*) between the predicted brain age and chronological age is computed, and statistical significance (P-value<0.05) - after adjustment for multiple comparisons using the FDR method - is denoted by the * symbol. Error bars represent the 95% confidence interval (CI). **D**) Scatter plot for the predicted brain age and chronological age. **E**) Phenotypic correlation (p_c) between the GM, WM, and FC-BAG using Pearson's correlation coefficient (*r*).

162 **GM, WM, and FC-BAG are associated with sixteen genomic loci**

163 In the European ancestry populations, GWAS (**Method 4A**) revealed 6, 9, and 1 genomic loci
164 linked to GM (N=31,557), WM (N=31,674), and FC-BAG (N=32,017), respectively (**Fig. 2A**).
165 The top lead SNP and mapped genes of each locus are presented in **Supplementary eTable 2**.
166 We also calculated the genomic inflation factor (λ) and the linkage disequilibrium score
167 regression (LDSC) intercept (b)[36] to scrutinize the robustness of the GWAS of GM-BAG
168 (λ=1.118; b=1.0016±0.0078), WM-BAG (λ=1.124; b=1.0187±0.0073), and FC-BAG (λ=1.046;
169 b=1.0039±0.006). All LDSC intercepts were close to 1, indicating no substantial genomic
170 inflation. The individual Manhattan and QQ plots of the three GWASs are presented in
171 **Supplementary eFigure 3** and are also publicly available at the MEDICINE knowledge portal:
172 https://labs.loni.usc.edu/medicine. The three BAGs were significantly heritable (P-value<$1\times10^{-}$
173 ^{10}) after adjusting for multiple comparisons using the Bonferroni method using the genome-wide
174 complex trait analysis (GCTA) software[37]. GM-BAG showed the highest SNP-based heritability
175 (h^2=0.47±0.02), followed by WM-BAG (h^2=0.46±0.02) and FC-BAG (h^2=0.11±0.02).

176 We performed a query in the GWAS Catalog[38] for these genetic variants within each
177 locus to understand the phenome-wide association of these identified loci in previous literature
178 (**Method 4C**). Notably, the SNPs within each locus were linked to other traits previously
179 reported in the literature (**Supplementary eFile 1**). Specifically, the GM-BAG loci were
180 uniquely associated with neuropsychiatric disorders such as major depressive disorder (MDD),
181 heart disease, and cardiovascular disease. We also observed associations between these loci and
182 other diseases (including anemia), as well as biomarkers from various human organs (e.g., liver)
183 (**Fig. 2B**). We then performed positional and functional annotations to map SNPs to genes
184 associated with GM, WM, and FC-BAG loci (**Method 4B**). **Fig. 2C-E** showcased the regional

185 Manhattan plot of one genomic locus linked to GM, WM, and FC-BAG. A detailed discussion of
186 these exemplary loci, SNPs, and genes is presented in **Supplementary eText 1**.
187 Finally, we calculated the genetic correlation (g_c) between the GM, WM, and FC-BAG
188 using the LDSC software. GM-BAG and WM-BAG showed the highest positive correlation
189 (g_c=0.49; P-value<1x10^{-10}); GM-BAG (g_c=0.20; P-value=0.025) and WM-BAG (g_c=0.29; P-
190 value=0.005) showed weak correlations with FC-BAG (**Fig. 2F**). The genetic correlations largely
191 mirror the phenotypic correlations, supporting the long-standing Cheverud's Conjecture[39]. We
192 also verified that these genetic correlations exhibited consistency between the two random splits
193 (split1 and spit2: 15,778<*N*<16,008), sharing a similar age and sex distribution (**Supplementary**
194 **eFigure 2**).
195
196 **Sensitivity analyses for the genome-wide associations**
197 We aimed to check the robustness of the main GWASs using the full sample sizes of the
198 European populations (**Fig. 2A**). To this end, we performed six sensitivity analyses (**Method**
199 **4A**).
200 Applying the Bonferroni method to correct for multiple comparisons, we noted high
201 concordance rates between the split1 (as discovery, 15,778<*N*<16,008) and split2 (as replication,
202 15,778<*N*<16,008) GWASs. Specifically, for GM-BAG, we observed a concordance rate of 99%
203 [P-value<0.05/3092; 3092 significant SNPs passing the genome-wide P-value threshold (<5x10^{-}
204 ^{8}) in the discovery data], and for WM-BAG, the concordance rate reached 100% (P-
205 value<0.05/116). FC-BAG did not achieve significant genome-wide results in the spit-sample
206 GWASs (**Supplementary eFigure 3** and **Supplementary eFile 2**).

207 In sex-stratified GWASs, the concordance rates were 100% (P-value<0.05/3072) for GM-
208 BAG and 88.6% (P-value<0.05/116) for WM-BAG when comparing the male-GWAS (as
209 replication, 14,969<*N*<15,127) to female-GWAS (as discovery, 16,588<*N*<16,890). FC-BAG
210 did not achieve significant genome-wide results (**Supplementary eFigure 4** and
211 **Supplementary eFile 3**).
212 The concordance rates of the GWASs using non-European ancestry populations (as
213 replication, 4646<*N*<5091) were low compared to the main GWASs using the European
214 population: only 13.78% for GM-BAG and 41.94% for WM-BAG (P-value<0.05)
215 (**Supplementary eFigure 5** and **Supplementary eFile 4**).
216 A mixed linear model employed via fastGWA[40] (as replication, 31,557<*N*<32,017)
217 obtained 100% concordance rates for GM, WM, and FC-BAG compared to GWAS using PLINK
218 linear regression (**Supplementary eFile 5**). The genetic loci, genomic inflation factor (λ), and
219 the LDSC intercepts for GM, WM, and FC-BAG were similar between the PLINK and fastGWA
220 analyses (**Supplementary eFigure 6**).
221 We found a 100% concordance rate of the SNPs identified for the GM-BAG GWAS
222 using LASSO regression (as discovery, BAG MAE=4.39 years) and SVR (P-value < 0.05/3382,
223 as replication, BAG MAE=4.43 years) (**Supplementary eFigure 7** and **Supplementary eFile**
224 **6**). The BAGs derived from the two machine larning models were highly correlated (*r*=0.99; P-
225 value<$1x10^{-10}$).
226 We finally found a 92.43% concordance rate of the SNPs identified in the GM-BAG
227 GWAS using the 119 MUSE ROIs[41] (as discovery, BAG MAE=4.39 years) and voxel-wide
228 RAVENS[42] maps (as replication, P-value < 0.05/3382, BAG MAE=5.12 years) (**Supplementary**
229 **eFigure 8** and **Supplementary eFile 7**). The BAGs derived from the two types of features were

230 significantly correlated (r=0.74; P-value<$1x10^{-10}$). The brain age prediction performance using
231 RAVENS showed marginal overfitting, with an MAE of 4.31 years in the training/validation/test
232 dataset and an MAE of 5.12 years in the independent test dataset.

233 These findings suggest that our GWASs were robust across sex, random splits, imaging
234 features, GWAS methods, and machine learning methods within European populations;
235 however, their generalizability to non-European populations is limited. All subsequent post-
236 GWAS analyses were conducted using the main GWAS results of European ancestry.

Figure 2: **Genome-wide associations of multimodal brain age gaps**

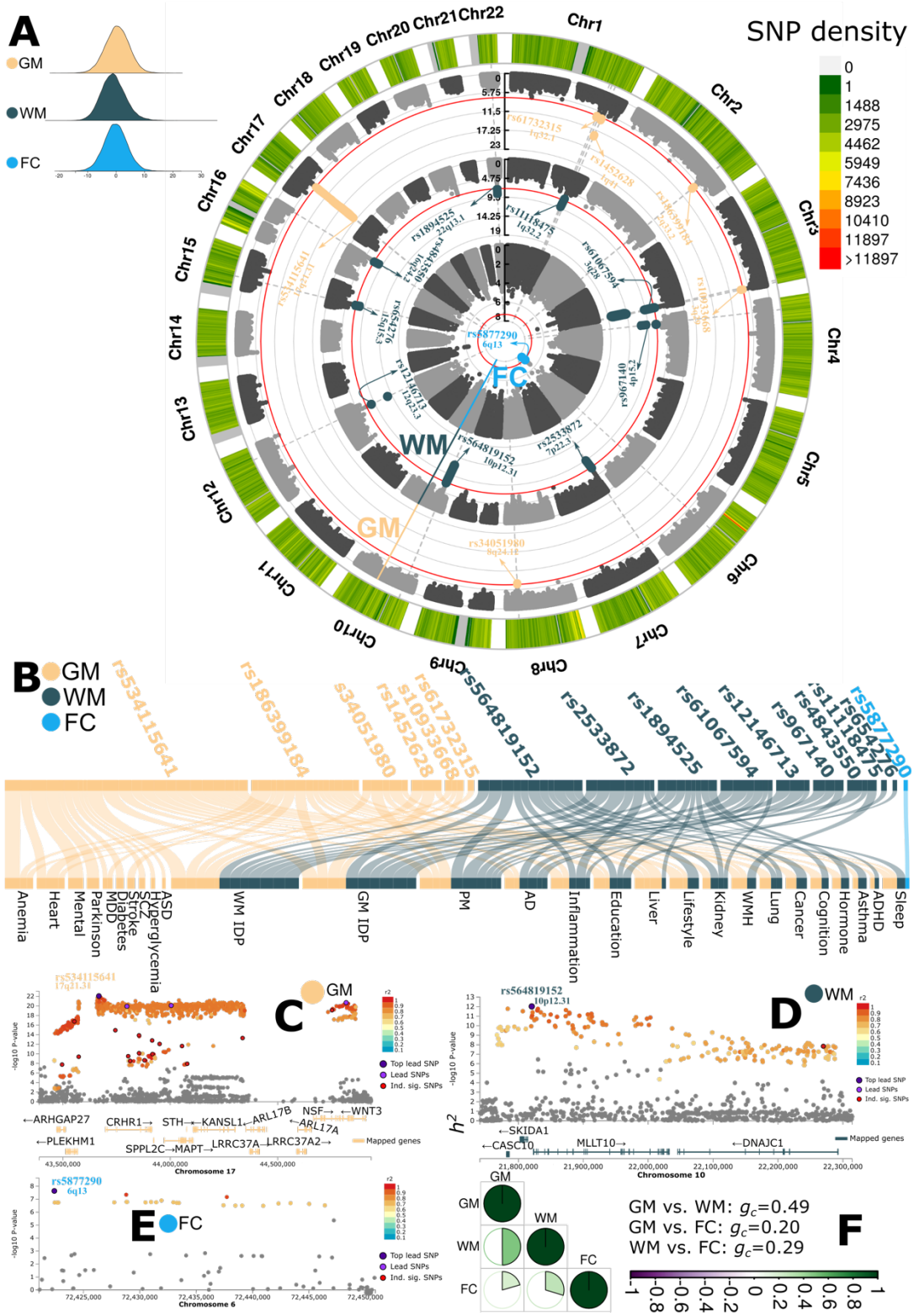

A) Genome-wide associations identified sixteen genomic loci associated with GM (6), WM (9), and FC-BAG (1) using a genome-wide P-value threshold [$-\log_{10}$(P-value) > 7.30]. The top lead

241 SNP and the cytogenetic region number represent each locus. **B**) Phenome-wide association
242 query from GWAS Catalog[38]. Independent significant SNPs inside each locus were largely
243 associated with many traits. We further classified these traits into several trait categories,
244 including biomarkers from multiple body organs (e.g., heart and liver), neurological disorders
245 (e.g., Alzheimer's disease and Parkinson's disease), and lifestyle risk factors (e.g., alcohol
246 consumption). **C**) Regional plot for a genomic locus associated with GM-BAG. Color-coded
247 SNPs are decided based on their highest r^2 to one of the nearby independent significant SNPs.
248 Gray-colored SNPs are below the r^2 threshold. The top lead SNP, lead SNPs, and independent
249 significant SNPs are denoted as dark purple, purple, and red, respectively. Mapped, orange-
250 colored genes of the genomic locus are annotated by positional, eQTL, and chromatin interaction
251 mapping (**Method 4B**). **D**) Regional plot for a genomic locus associated with WM-BAG. **E**) The
252 novel genomic locus associated with FC-BAG did not map to any genes. We used the Genome
253 Reference Consortium Human Build 37 (GRCh37) in all genetic analyses. **F**) Genetic correlation
254 (g_c) between the GM, WM, and FC-BAG using the LDSC software. Abbreviation: AD:
255 Alzheimer's disease; ASD: autism spectrum disorder; PD: Parkinson's disease; ADHD: attention-
256 deficit/hyperactivity disorder.
257

258 **The gene-drug-disease network highlights disease-specific drugs that bind to genes**

259 **associated with GM and WM-BAG**

260 We investigated the potential "druggable genes[43]" from the mapped genes by constructing a

261 gene-drug-disease network (**Method 4F**). The network connects genes with drugs (or drug-like

262 molecules) targeting specific diseases currently active at any stage of clinical trials.

263 We revealed clinically relevant associations for 4 and 6 mapped genes associated with

264 GM-BAG and WM-BAG, respectively. The GM-BAG genes were linked to clinical trials for

265 treating heart, neurodegenerative, neuropsychiatric, and respiratory diseases. On the other hand,

266 the WM-BAG genes were primarily targeted for various cancer treatments and cardiovascular

267 diseases (**Fig. 3**). To illustrate, for the GM-BAG *MAPT* gene, several drugs or drug-like

268 molecules are currently being evaluated for treating AD. Semorinemab (RG6100), an anti-tau

269 IgG4 antibody, was being investigated in a phase-2 clinical trial (trial number: NCT03828747),

270 which targets extracellular tau in AD, to reduce microglial activation and inflammatory

271 responses[44]. Another drug is the LMTM (TRx0237) - a second-generation tau protein

272 aggregation inhibitor currently being tested in a phase-3 clinical trial (trial number:
273 NCT03446001) for treating AD and frontotemporal dementia[45]. Regarding WM-BAG genes,
274 they primarily bind with drugs for treating cancer and cardiovascular diseases. For instance, the
275 *PDIA3* gene, associated with the folding and oxidation of proteins, has been targeted for
276 developing several zinc-related FDA-approved drugs for treating cardiovascular diseases.
277 Another example is the *MAP1A* gene, which encodes microtubule-associated protein 1A. This
278 gene is linked to the development of estramustine, an FDA-approved drug for prostate cancer
279 (**Fig. 3**). Detailed results are presented in **Supplementary eFile 8**.

Figure 3: **Gene-drug-disease network of multimodal brain age gaps**

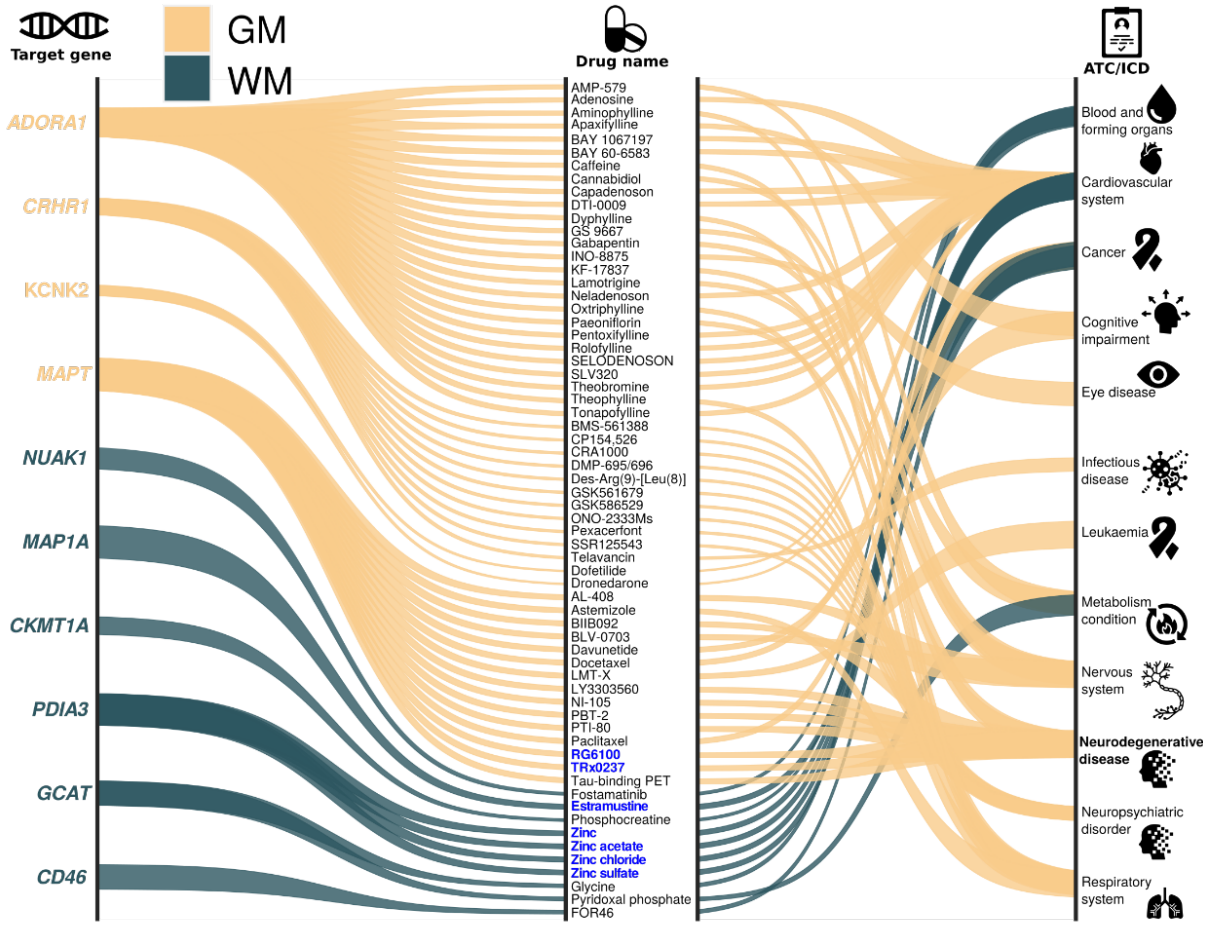

The gene-drug-disease network derived from the mapped genes revealed a broad spectrum of targeted diseases and cancer, including brain cancer, cardiovascular system diseases, Alzheimer's disease, and obstructive airway disease, among others. The thickness of the lines represented the P-values ($-\log_{10}$) from the brain tissue-specific gene set enrichment analyses using the GTEx v8 dataset. We highlight several drugs under the blue-colored and bold text. Abbreviation: ATC: Anatomical Therapeutic Chemical; ICD: International Classification of Diseases.

Multimodal BAG is genetically correlated with AI-derived subtypes of brain diseases

We calculated the genetic correlation using the GWAS summary statistics from 16 clinical traits to examine genetic covariance between multimodal BAG and other clinical traits. The selection procedure and quality check of the GWAS summary statistics are detailed in **Method 4D**. These traits encompassed common brain diseases and their AI-derived disease subtypes, as well as education and intelligence (**Fig. 4A** and **Supplementary eTable 3**). The AI-generated disease

295 subtypes were established in our previous studies utilizing semi-supervised clustering methods[46]
296 and IDP from brain MRI scans.
297 Our analysis revealed significant genetic correlations between GM-BAG and AI-derived
298 subtypes of AD (AD1[4]), autism spectrum disorder (ASD) (ASD1 and ASD3[47]), schizophrenia
299 (SCZ1[48]), and obsessive-compulsive disorder (OCD)[49]; WM-BAG and AD1, ASD1, SCZ1, and
300 SCZ2; and FC-BAG and education[50] and SCZ1. Detailed results for r_g estimates are presented in
301 **Supplementary eTable 4**. These subtypes, in essence, capture more homogeneous disease
302 effects than the conventional "unitary" disease diagnosis, hence serving as robust
303 endophenotypes[23].
304
305 **Multimodal BAG shows specific enrichment of heritability in different functional**
306 **categories and cell types**
307 We conducted a partitioned heritability analysis[51] to investigate the heritability enrichment of
308 genetic variants related to multimodal BAG in the 53 functional categories (**Method 4E**). Our
309 results revealed that GM and WM-BAG exhibited significant heritability enrichment across
310 numerous annotated functional categories. Specifically, some categories displayed greater
311 enrichment than others, and we have outlined some in further detail.
312 For GM-BAG, the regions conserved across mammals, as indicated by the label
313 "conserved" in **Fig. 4B**, displayed the most notable enrichment of heritability: approximately
314 2.61% of SNPs were found to explain 0.43±0.07 of SNP heritability (P-value=5.80×10^{-8}).
315 Additionally, transcription start site (TSS)[52] regions employed 1.82% of SNPs to explain
316 0.16±0.05 of SNP heritability (P-value=8.05×10^{-3}). TSS initiates the transcription at the 5' end of
317 a gene and is typically embedded within a core promoter crucial to the transcription machinery[53].

318 The heritability enrichment of Histone H3 at lysine 4, as denoted for "H3K4me3_peaks" in **Fig.**
319 **4B**, and histone H3 at lysine 9 (H3K9ac)[54] were also found to be large and were known to
320 highlight active gene promoters[55]. For WM-BAG, 5' untranslated regions (UTR) used 0.54% of
321 SNPs to explain 0.09±0.03 of SNP heritability (P-value=4.24×10^{-3}). The 5' UTR is a crucial
322 region of a messenger RNA located upstream of the initiation codon. It is pivotal in regulating
323 transcript translation, with varying mechanisms in viruses, prokaryotes, and eukaryotes.
324 Additionally, we examined the heritability enrichment of multimodal BAG in three
325 different cell types (**Fig. 4C**). WM-BAG (P-value=1.69×10^{-3}) exhibited significant heritability
326 enrichment in oligodendrocytes, one type of neuroglial cells. FC-BAG (P-value=1.12×10^{-2})
327 showed such enrichment in astrocytes, the most prevalent glial cells in the brain. GM-BAG
328 showed no enrichment in any of these cells. Our findings are consistent with understanding the
329 molecular and biological characteristics of GM and WM. Oligodendrocytes are primarily
330 responsible for forming the lipid-rich myelin structure, whereas astrocytes play a crucial role in
331 various cerebral functions, such as brain development and homeostasis. Convincingly, a prior
332 GWAS[14] on WM-IDP also identified considerable heritability enrichment in glial cells,
333 especially oligodendrocytes. Detailed results for the 53 functional categories and cell-specific
334 analyses are presented in **Supplementary eTable 5**.
335

336 **Prediction ability of the polygenic risk score of the multimodal BAG**

337 We derived the PRS for GM, WM, and FC-BAG using the conventional C+T (clumping plus P-
338 value threshold) approach[56] via PLINK and a Bayesian method via PRS-CS[57] (**Method 4H**).
339 We found that the GM, WM, and FC-BAG-PRS derived from PRS-CS significantly
340 predicted the phenotypic BAGs in the test data (split2 GWAS, $15{,}697 < N < 15{,}940$), with an

341 incremental R^2 of 2.17%, 1.85%, and 0.19%, respectively (**Fig. 4D**). Compared to the PRS
342 derived from PRS-CS, the PLINK approach achieved a lower incremental R^2 of 0.81%, 0.45%,
343 and 0.14% for GM, WM, and FC-BAG, respectively (**Supplementary eFigure 9**). Overall, the
344 predictive capacity of PRS is moderate, in line with earlier discoveries involving raw imaging-
345 derived phenotypes, as demonstrated in Zhao et al.[13], where PRSs developed for seven selective
346 brain regions were able to explain roughly 1.18% to 3.93% of the phenotypic variance associated
347 with these traits.

Figure 4: **Genetic correlation, partitioned heritability enrichment, and PRS prediction accuracy on multimodal brain age gaps**

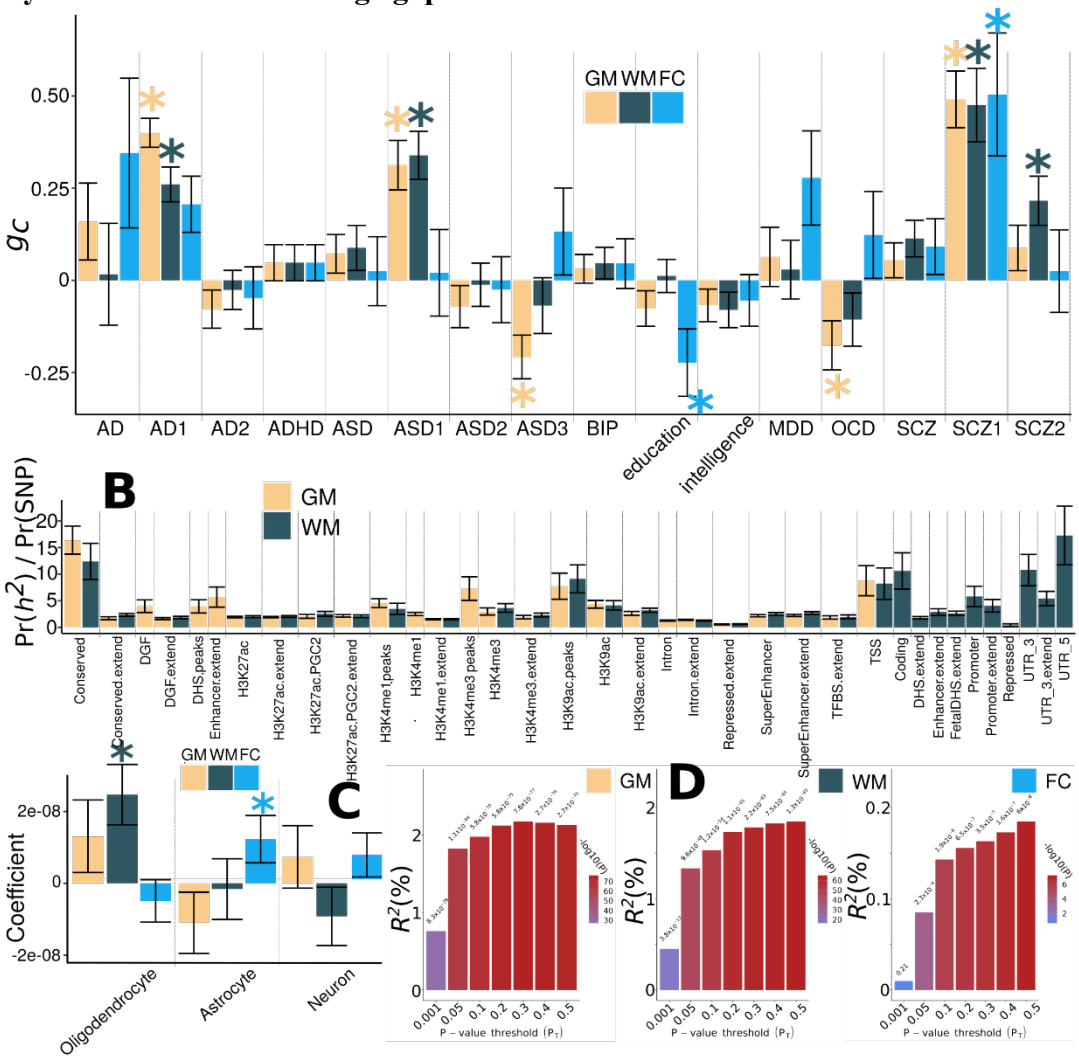

A) Genetic correlation (g_c) between GM, WM, and FC-BAG and 16 clinical traits. These traits include neurodegenerative diseases (e.g., AD) and their AI-derived subtypes (e.g., AD1 and AD2[4]), neuropsychiatric disorders (e.g., ASD) and their subtypes (ASD1, 2, and 3[47]), intelligence, and education. **B**) The proportion of heritability enrichment for the 53 functional categories[51]. We only show the functional categories that survived the correction for multiple comparisons using the FDR method. **C**) Cell type-specific partitioned heritability estimates. We included gene sets from Cahoy et al.[58] for three main cell types (i.e., astrocyte, neuron, and oligodendrocyte). After adjusting for multiple comparisons using the FDR method, the * symbol denotes statistical significance (P-value<0.05). Error bars represent the standard error of the estimated parameters. **D**) The incremental R^2 of the PRS derived by PRC-CS to predict the GM, WM, and FC-BAG in the target/test data (i.e., the split2 GWAS). The *y*-axis indicates the proportions of phenotypic variation (GM, WM, and FC-BAG) that the PRS can significantly and additionally explain. The *x*-axis lists the seven P-value thresholds considered. Abbreviation: AD: Alzheimer's disease; ADHD: attention-deficit/hyperactivity disorder; ASD: autism spectrum disorder; BIP: bipolar disorder; MDD: major depressive disorder; OCD: obsessive-compulsive disorder; SCZ: schizophrenia; CAD: coronary artery disease; CD: Crohn's disease; BMD: bone

367 mineral density; PD: Parkinson's disease; SLE: systemic lupus erythematosus; BMI: body mass
368 index; CVD: cardiovascular disease; LDL: low-density lipoprotein cholesterol; MS: multiple
369 sclerosis; AF: Atrial fibrillation.
370

371 **The potential causal relationships between GM and WM-BAG and other clinical traits**

372 We investigated the potential causal effects of several risk factors (i.e., exposure variable) on
373 multimodal BAG (i.e., outcome variable) using a bidirectional two-sample MR approach[59]
374 (**Method 4G**). We hypothesized that several diseases and lifestyle risk factors might contribute
375 to accelerating or decelerating human brain aging.

376 We found putative causal effects of triglyceride-to-lipid ratio in very large very-low-
377 density lipoprotein (VLDL)[60] [P-value=5.09×10^{-3}, OR (95% CI) = 1.08 (1.02, 1.13), number of
378 SNPs=52], type 2 diabetes[61] [P-value=1.96×10^{-2}, OR (95% CI) = 1.05 (1.01, 1.09), number of
379 SNPs=10], and breast cancer[62] [P-value=1.81×10^{-2}, OR (95% CI) = 0.96 (0.93, 0.99), number of
380 SNPs=118] on GM-BAG (i.e., accelerated brain age). We also identified causal effects of AD[63]
381 [P-value=7.18×10^{-5}, OR (95% CI) = 1.04 (1.02, 1.05), number of SNPs=13] on WM-BAG (**Fig.
382 5A**). We subsequently examined the potential inverse causal effects of multimodal BAG (i.e.,
383 exposure) on these risk factors (i.e., outcome). However, owing to the restricted power [number
384 of instrumental variables (IV) < 6], we did not observe any significant signals (**Supplementary
385 eFigure 10** and **Supplementary eFile 9**).
386

387 **Sensitivity analyses for Mendelian randomization**

388 We performed sensitivity analyses to investigate potential violations of the three IV assumptions
389 (**Method 4G**). To illustrate this, we showcased the sensitivity analysis results for the causal
390 effect of the triglyceride-to-lipid in VLDL ratio on GM-BAG (**Fig. 5B-E**). In a leave-one-out
391 analysis, we found that no single SNP overwhelmingly drove the overall effect (**Fig. 5B**). There

392 was evidence for the presence of minor heterogeneity[64] of the causal effect amongst SNPs
393 (Cochran's Q value=76.06, P-value=5.09×10^{-3}). Some SNPs exerted opposite causal effects
394 compared to the model using all SNPs (**Fig. 5C**). The scatter plot (**Fig. 5D**) indicated one
395 obvious SNP outlier (rs11591147), and the funnel plot showed little asymmetry with only an
396 outlier denoted in **Fig. 5E** (rs4507142). Finally, the MR Egger estimator allows for pleiotropic
397 effects independent of the effect on the exposure of interest (i.e., the InSIDE assumption[65]). Our
398 results from the Egger estimator showed a small positive intercept ($5.21 \times 10^{-3} \pm 2.87 \times 10^{-3}$, P-
399 value=0.07) and a lower OR [inverse-variance weighted (IVW): 1.08 (1.02, 1.13) vs. Egger: 1.01
400 (0.93, 1.10)], which may indicate the presence of directional horizontal pleiotropy for some
401 SNPs. We present sensitivity analyses for other significant exposure variables in **Supplementary**
402 **eFigure 11**.
403 To investigate the potential directional pleiotropic effects, we re-analyzed the MR Egger
404 regression by excluding the two outliers identified in **Fig. 5D** (rs11591147) and **E** (rs4507142),
405 which led to a slightly increased OR [1.04 (0.96, 1.12)] and a smaller positive intercept ($4.41 \times 10^{-}$
406 $^{3} \pm 2.65 \times 10^{-3}$, P-value=0.09). Our findings support that these two outlier SNPs may have a
407 directional pleiotropic effect on GM-BAG. Nevertheless, given the complex nature of brain
408 aging, many other biological pathways may also contribute to human brain aging. For instance,
409 the SNP (rs11591147) was largely associated with other blood lipids, such as LDL cholesterol[66],
410 and heart diseases, such as coronary artery disease[67]. Detailed results obtained from all five MR
411 methods are presented in **Supplementary eFile 9**.
412

Figure 5: **Causal inference of multimodal brain age gaps**

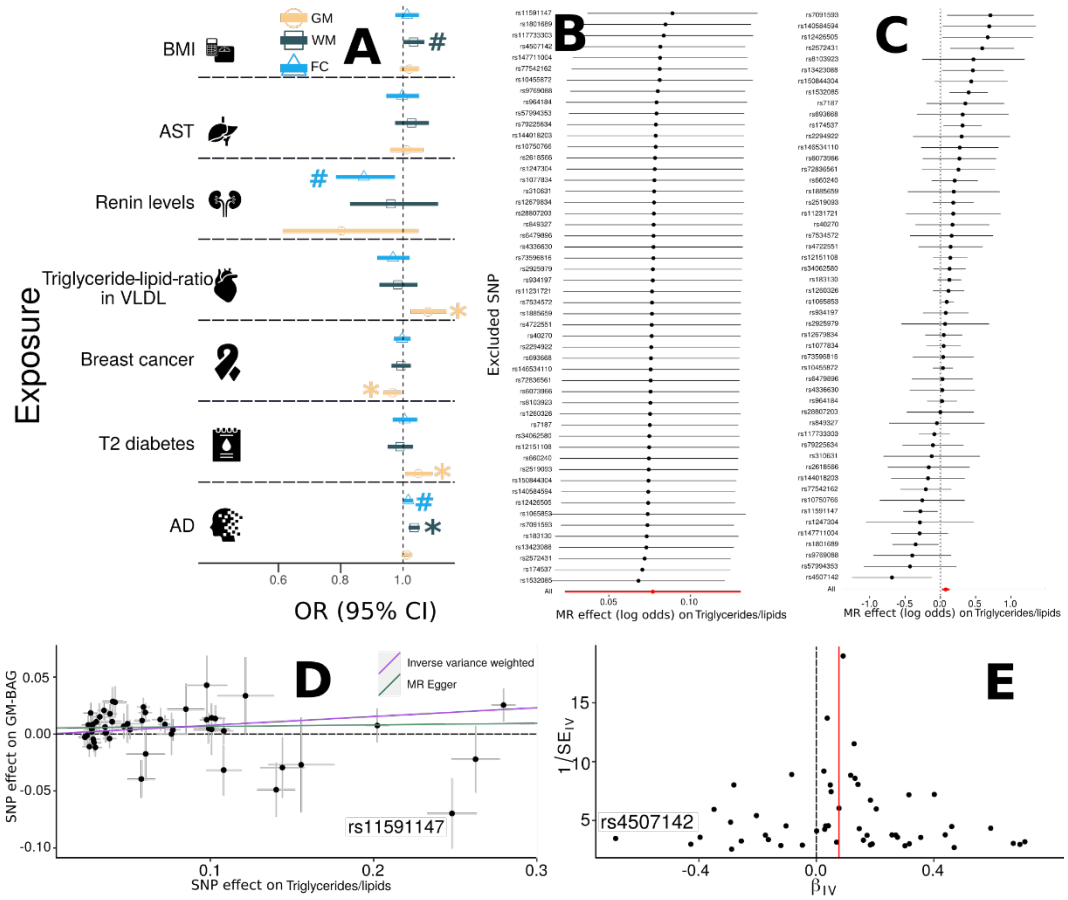

A) Causal inference was performed using a two-sample Mendelian Randomization (MR, **Method 4G**) approach for seven selected exposure variables on three outcome variables (i.e., GM, WM, and FC-BAG). The symbol * denotes statistical significance after correcting for multiple comparisons using the FDR method (*N*=7); the symbol # denotes the tests passing the nominal significance threshold (P-value=0.05) but did not survive the multiple comparisons. The odds ratio (OR) and the 95% confidence interval (CI) are presented. **B**) Leave-one-out analysis of the triglyceride-to-lipid ratio on GM-BAG. Each row represents the MR effect (log OR) and the 95% CI by excluding that SNP from the analysis. The red line depicts the IVW estimator using all SNPs. **C**) Forest plot for the single-SNP MR results. Each line represents the MR effect (log OR) for the triglyceride-to-lipid ratio on GM-BAG using only one SNP; the red line shows the MR effect using all SNPs together. **D**) Scatter plot for the MR effect sizes of the SNP-triglyceride-to-lipid ratio association (*x*-axis, SD units) and the SNP-GM-BAG associations (*y*-axis, log OR) with standard error bars. The slopes of the purple and green lines correspond to the causal effect sizes estimated by the IVW and the MR Egger estimator, respectively. We annotated a potential outlier. **E**) Funnel plot for the relationship between the causal effect of the triglyceride-to-lipid ratio on GM-BAG. Each dot represents MR effect sizes estimated using each SNP as a separate instrument against the inverse of the standard error of the causal estimate. The vertical red line shows the MR estimates using all SNPs. We annotated a potential outlier. Abbreviation: AD: Alzheimer's disease; AST: aspartate aminotransferase; BMI: body mass

index; VLDL: very low-density lipoprotein; CI: confidence interval; OR: odds ratio; SD: standard deviation; SE: standard error.

Discussion

The present study harnessed brain imaging genetics from a cohort of 42,089 participants in UKBB to investigate the underlying genetics of multimodal BAG. Our approach commenced with objectively assessing brain age prediction performance, encompassing various imaging modalities (T1-weighted, diffusion, and resting-state MRI), feature types (ROI vs. voxel), and machine learning algorithms. Subsequently, we conducted genome-wide associations, demonstrating the robustness of identified genetic signals in individuals of European ancestry across diverse factors. Lastly, our study encompassed several post-GWAS analyses, validating the GWAS results, shedding light on the intricate biological processes involved, and uncovering the multifaceted interplay between human brain aging and various health conditions and clinical traits. Our findings unveiled shared genetic factors and unique characteristics – varying degrees of phenotypic and genetic correlation – within BAG across three distinct imaging modalities.

Genetic architecture of GM-BAG

Our genetic results from GM-BAG substantiate that many diseases, conditions, and clinical phenotypes share genetic underpinnings with brain age, perhaps driven by macrostructural changes in GM (e.g., brain atrophy). The locus with the most significant signal (the top lead SNP rs534114641 at 17q21.31) showed substantial association with the traits mentioned above and was mapped to numerous genes associated with various diseases (**Fig. 2C**). Several previous GM-BAG GWAS[20,22] also identified this locus. Among these genes, the *MAPT* gene, known to encode a protein called tau, is a prominent AD hallmark and implicated in approximately 30 tauopathies, including progressive supranuclear palsy and frontotemporal lobar degeneration[68]. Our gene-drug-disease network also showed several drugs, such as Semorinemab[44], in active clinical trials currently targeting treatment for AD (**Fig. 3**). The

460 heritability enrichment of GM-BAG was high in several functional categories, with conserved
461 regions being the most prominent. The observed higher heritability enrichment in conserved
462 regions compared to coding regions[69] supports the long-standing hypothesis regarding the
463 functional significance of conserved sequences. However, the precise role of many highly
464 conserved non-coding DNA sequences remains unclear[70]. The genetic correlation results of GM-
465 BAG with subtypes of common brain diseases highlight the promise for the AI-derived subtypes,
466 rather than the "one-for-all" unitary disease diagnosis, as robust endophenotypes[23]. These
467 findings strongly support the clinical implications of re-evaluating pertinent hypotheses using the
468 AI-derived subtypes in patient stratification and personalized medicine.

469 The elevated triglyceride-to-lipid ratio in VLDL, an established biomarker for
470 cardiovascular diseases[71], is causally associated with higher GM-BAG (accelerated brain age).
471 Therefore, lifestyle interventions that target this biomarker might hold promise as an effective
472 strategy to enhance overall brain health. In addition, we revealed that one unit-increased
473 likelihood of type 2 diabetes has a causal effect on GM-BAG increase. Research has shown that
474 normal brain aging is accelerated by approximately 26% in patients with progressive type 2
475 diabetes compared with healthy controls[72]. The protective causal effect of breast cancer on GM-
476 BAG is intriguing in light of existing literature adversely linking breast cancer to brain
477 metastasis[73] and chemotherapy-induced cognitive impairments, commonly known as "chemo
478 brain". In addition, it's important to exercise caution when considering the potential causal link
479 between breast cancer and GM-BAG, as MR analyses are susceptible to population selection
480 bias[74] due to the high breast cancer mortality rate.

481 **Genetic architecture of WM-BAG**

482 The genetic architecture of WM-BAG exhibits strong correlations with cancer-related
483 traits, AD, and physical measures such as BMI, among others. Our phenome-wide association
484 query largely confirms the enrichment of these traits in previous literature. In particular, the
485 *DNAJC1* gene, annotated from the most polygenic locus on chromosome 10 (top lead SNP:
486 rs564819152), encodes a protein called heat shock protein 40 (Hsp40) and plays a role in protein
487 folding and the response to cellular stress. This gene is implicated in various cancer types, such
488 as breast, renal, and melanoma (**Supplementary eFigure 12**). In addition, several FDA-
489 approved drugs have been developed based on these WM-BAG genes for different types of
490 cancer in our gene-drug-disease network (**Fig. 3**). Our findings provide novel insights into the
491 genetic underpinnings of WM-BAG and their potential relevance to cancer.
492 Remarkably, one unit-increased likelihood of AD was causally associated with increased
493 WM-BAG. Our Mendelian randomization analysis confirmed the abundant association
494 evidenced by the phenome-wide association query (**Fig. 2B**). Dementia, such as AD, is
495 undeniably a significant factor contributing to the decline of the aging brain. Evidence suggests
496 that AD is not solely a GM disease; significant microstructural changes can be observed in WM
497 before the onset of cognitive decline[75]. We also identified a nominal causal significance of BMI
498 [risk effect; P-value=4.73×10^{-2}, OR (95% CI) = 1.03 (1.00, 1.07)] on WM-BAG. These findings
499 underscore the potential of lifestyle interventions and medications currently being tested in
500 clinical trials for AD to improve overall brain health.
501 **Genetic architecture of FC-BAG**
502 The genetic signals for FC-BAG were weaker than those observed for GM and WM-
503 BAG, which is consistent with the age prediction performance and partially corroborates
504 Cheverud's conjecture: using genetic correlations (**Fig. 2F**) as proxies for phenotypic correlations

505 (**Fig. 1E**) when collecting individual phenotypes is expensive and unavailable. A novel genomic
506 locus on chromosome 6 (6q.13) harbors an independent variant (rs1204329) previously linked to
507 insomnia[76]. The top lead SNP, rs5877290, associated with this locus is a novel deletion-insertion
508 mutation type: no known association with any human disease or gene mapping has been
509 established for this SNP. The genetic basis of FC-BAG covaries with educational performance
510 and schizophrenia subtypes. Specifically, parental education has been linked to cognitive ability,
511 and researchers have identified a functional connectivity biomarker between the right rostral
512 prefrontal cortex and occipital cortex that mediates the transmission of maternal education to
513 offspring's performance IQ[77]. On the other hand, schizophrenia is a highly heritable mental
514 disorder that exhibits functional dysconnectivity throughout the brain[78]. AD was causally
515 associated with FC-BAG with nominal significance [risk effect for per unit increase; P-
516 value=4.43×10^{-2}, OR (95% CI) = 1.02 (1.00, 1.03), number of SNPs=13] (**Fig. 5A**). The
517 relationship between functional brain networks and the characteristic distribution of amyloid-β
518 and tau in AD[79] provides evidence that AD is a significant factor in the aging brain, underscoring
519 its role as a primary causative agent.

520 The comparative trend of genetic heritability among GM, WM, and FC-BAG is also
521 consistent with previous large-scale GWAS of multimodal brain IDP. Zhao et al. performed
522 GWAS on GM[13], WM[14], and FC-IDP[18], showing that FC-IDP is less genetically heritable than
523 others. Similar observations were also demonstrated by Elliot et al.[11] in the first large-scale
524 GWAS using multimodal IDP from UKBB. The weaker genetic signal observed in FC-BAG can
525 be attributed to many factors. One of the main reasons is the higher signal-to-noise ratio in FC
526 measurements due to the dynamic and complex nature of brain activity, which can make it
527 difficult to accurately measure and distinguish between the true signal and noise. Social-

528 environmental and lifestyle factors can also contribute to the "missing heritability" observed in
529 FC-BAG. For example, stress, sleep patterns, physical activity, and other environmental factors
530 can impact brain function and connectivity[80]. In contrast, GM and WM measurements are more
531 stable and less influenced by environmental factors, which may explain why they exhibit
532 stronger genetic signals and higher heritability estimates.
533
534 **Limitations**
535 This study has several limitations. We can employ deep learning on voxel-wise imaging scans to
536 enhance brain age prediction performance. Nevertheless, it warrants additional exploration to
537 determine whether the resulting reduction in MAE translates into more robust genome-wide
538 associations, as our previous work has demonstrated that BAGs derived from a CNN with a
539 lower MAE did not exhibit heightened sensitivity to disease effects such as AD[35]. Second, the
540 generalization ability of the GWAS findings to non-European ancestry is limited, potentially due
541 to small sample sizes and cryptic population stratification. Future investigations can be expanded
542 to encompass a broader spectrum of underrepresented ethnic groups, diverse disease populations,
543 and various age ranges spanning the entire lifespan. This expansion can be facilitated by
544 leveraging the resources of large-scale brain imaging genetic consortia like ADNI[81], focused on
545 Alzheimer's disease, and ABCD[82], which centers on brain development during adolescence.
546 Third, it's important to exercise caution when interpreting the results of this study due to the
547 various assumptions associated with the statistical methods employed, including LDSC and MR.
548 Lastly, it's worth noting that brain age represents a residual score encompassing measurement
549 error. A recent study[83] has underscored the significance of incorporating longitudinal data when

550 calculating brain age. Future research should be conducted once the longitudinal scans from the
551 UK Biobank become accessible to explore this impact on GWASs.
552
553 **Outlook**
554 In summary, our multimodal BAG GWASs provide evidence that the aging process of the
555 human brain is a complex biological phenomenon intertwined with several organ systems and
556 chronic diseases. We digitized the human brain from multimodal imaging and captured a
557 complete genetic landscape of human brain aging. This opens new avenues for drug
558 repurposing/repositioning and aids in identifying modifiable protective and risk factors that can
559 ameliorate human brain health.
560

Methods

Method 1: Study populations

UKBB is a population-based study of more than 50,000 people recruited between 2006 and 2010 from Great Britain. The current study focused on participants from the imaging-genomics population who underwent both an MRI scan and genome sequencing (genotype array data and the imputed genotype data) under application number 35148. The UKBB study has ethical approval, and the ethics committee is detailed here: https://www.ukbiobank.ac.uk/learn-more-about-uk-biobank/governance/ethics-advisory-committee. The study design, phenotype and genetic data availability, and quality check have been published and detailed elsewhere[24]. **Table 1** shows the study characteristics of the present work.

To train the machine learning model and compare the performance of the multimodal BAG, we defined the following two datasets:

- *Training/validation/test dataset*: To objectively compare the age prediction performance of different MRI modalities and machine learning models, we randomly sub-sampled 500 (250 females) participants within each decade's range from 44 to 84 years old, resulting in the same 4000 participants for GM, WM, and FC-IDP. This dataset was used to train machine learning models. In addition, we ensured that the training/validation/test splits were the same in the CV procedure. As UKBB is a general population, we explicitly excluded participants with common brain diseases, including mental and behavioral disorders (ICD-10 code: F; *N*=2678) and diseases linked to the central nervous system (ICD-10 code: G group; *N*=3336).

582 • *Independent test dataset*: The rest of the population for each MRI modality
583 (*N*=38089) was set as independent test datasets – unseen until we finalized the
584 training procedure[84].

585 The GM-IDP includes 119 GM regional volumes from the MUSE atlas, consolidated by
586 the iSTAGING consortium. We studied the influence of different WM-IDP features: i) 48 FA
587 values; ii) 109 TBSS-based[85] values from FA, MD, ODI, and NDI; iii) 192 skeleton-based mean
588 values from FA, MD, ODI, and NDI. For FC-IDP, 210 ICA-derived functional connectivity
589 components were included. The WM and FC-IDP were downloaded from UKBB (**Method 3B**).

590 **Table 1. Study characteristics.**
591 The current table presents participants of all ancestries for the age prediction task. We
592 constrained participants with only European ancestry for downstream genetic analyses. * For age
593 and sex, we reported statistics for the overlapping population of the three modalities: 35,261
594 participants for the entire population, 4000 participants for the training/validation/test dataset,
595 and 31,261 participants for the independent test dataset. We also showed the number of
596 participants for the GM, WM, and FC-BAG GWAS. In total, our analyses included 42,089
597 unique participants who had at least one image scan. Abbreviation: dMRI: diffusion MRI;
598 rsfMRI: resting-state functional MRI; T1w MRI: T1-weighted MRI.
599

Population (overlap)	T1w MRI	dMRI	rsfMRI	Age (year)*	Sex /female*
Total (35,261)	36,304	39,661	36,858	63.64 (45.00, 81.00)	18,700/53%
Training/validation/test (4000)	4000	4000	4000	63.47 (46.00, 81.00)	2000/50%
Independent test (31,261)	32,304	35,661	32,858	63.66 (45.00, 81.00)	16,700/53%
GWAS	31,557	31,749	32,017	NA	NA

600

601 **Method 2: Image processing**

602 **(A): T1-weighted MRI processing**: The imaging quality check is detailed in **Supplementary**
603 **eMethod 2**. All images were first corrected for magnetic field intensity inhomogeneity.[86] A deep

604 learning-based skull stripping algorithm was applied to remove extra-cranial material. In total,
605 145 IDPs were generated in gray matter (GM, 119 ROIs), white matter (WM, 20 ROIs), and
606 ventricles (6 ROIs) using a multi-atlas label fusion method[41]. The 119 GM ROIs were fit to the
607 four machine learning models to derive the GM-BAG.
608
609 **(B): Diffusion MRI processing**: UKBB has processed diffusion MRI (dMRI) data and released
610 several WM tract-based metrics for the Diffusion Tensor Imaging (DTI) model (single-shell
611 dMRI) and Neurite Orientation Dispersion and Density Imaging (NODDI[87]) model (multi-shell
612 dMRI). The Eddy[88] tool corrected raw images for eddy currents, head motion, and outlier slices.
613 The mean values of FA, MD, ODI, and NDI were extracted from the 48 WM tracts of the
614 "ICBM-DTI-81 white-matter labels" atlas[89], resulting in 192 WM-IDP (category code:134). In
615 addition, a tract-skeleton (TBSS)[85] and probabilistic tractography analysis[90] were employed to
616 derive weighted-mean measures within the 27 major WM tracts, referred to as the 108 TBSS
617 WM-IDP (category code: 135). Finally, since we observed overfitting – an increase of MAEs
618 from the cross-validated test results to the independent test results – when incorporating features
619 from FA, MD, ODI, and NDI (as detailed in **Supplementary eTable 1A**), we chose to use only
620 the 48 FA WM-IDPs to train the models for generating GM-BAG.
621
622 **(C): Resting-state functional MRI processing**: For FC-IDP, we used the 21 × 21 resting-state
623 functional connectivity (full correlation) matrices (data-field code: 25750) from UKBB[91,92].
624 UKBB processed rsfMRI data and released 25 whole-brain spatial independent component
625 analysis (ICA)-derived components[93]; four components were removed due to artifactual
626 components. This resulted in 210 FC-IDP quantifying pairwise correlations of the ICA-derived

627 components. Details of dMRI and rsfMRI processing are documented here:

628 https://biobank.ctsu.ox.ac.uk/crystal/crystal/docs/brain_mri.pdf.

629

630 **Method 3: Multimodal brain age prediction using machine learning models**

631 GM, WM, and FC-IDP (details of image processing are presented in **Method 2**) were fit into

632 four machine learning models (linear and non-linear) to predict brain age as the outcome.

633 Specifically, we used SVR, LASSO regression, MLP, and a five-layer neural network (NN: three

634 linear layers and one rectified linear unit layer).

635 To objectively and reproducibly compare the age prediction performance using different

636 machine learning models and MRI modalities, we adopted a nested CV procedure and included

637 an independent test dataset[27]. Specifically, the outer loop CV was performed for 100 repeated

638 random splits: 80% of the data were used for training. The remaining 20% was used for

639 validation/testing in the inner loop with a 10-fold CV. In addition, we concealed an independent

640 test dataset – unseen for testing until we finished fine-tuning the machine learning models[84] (e.g.,

641 hyperparameters for SVR and neural networks). To compare the results of different models and

642 modalities, we showed MAE's mean and empirical standard deviation instead of performing any

643 statistical test (e.g., a two-sample t-test). This is because no unbiased variance estimate exists for

644 complex CV procedures (refer to notes from Nadeau and Benjio[94]).

645

646 **Method 4: Genetic analyses**

647 Imputed genotype data were quality-checked for downstream analyses. Our quality check

648 pipeline (see below) resulted in 33,541 European ancestry participants and 8,469,833 SNPs.

649 After merging with the multimodal MRI populations, we included 31,557 European participants

650 for GM-BAG, 31,749 participants for WM-BAG, and 32,017 participants for FC-BAG GWAS.
651 Details of the protocol are described elsewhere[15,95]. We summarize our genetic QC pipeline as
652 below. First, we excluded related individuals (up to 2nd-degree) from the complete UKBB
653 sample using the KING software for family relationship inference[96]. We then removed
654 duplicated variants from all 22 autosomal chromosomes. Individuals whose genetically identified
655 sex did not match their self-acknowledged sex were removed. Other excluding criteria were: i)
656 individuals with more than 3% of missing genotypes; ii) variants with minor allele frequency
657 (MAF) of less than 1%; iii) variants with larger than 3% missing genotyping rate; iv) variants
658 that failed the Hardy-Weinberg test at $1x10^{-10}$. To adjust for population stratification[97], we
659 derived the first 40 genetic principle components (PC) using the FlashPCA software[98]. Details of
660 the genetic quality check protocol are described elsewhere[95,99].
661
662 **(A): Genome-wide association analysis**: For GWAS, we ran a linear regression using Plink[100]
663 for GM, WM, and FC-BAG, controlling for confounders of age, dataset status
664 (training/validation/test or independent test dataset), age x squared, sex, age x sex interaction,
665 age-squared x sex interaction, total intracranial volume, the brain position in the scanner (lateral,
666 transverse, and longitudinal), and the first 40 genetic principal components. The inclusion of
667 these covariates is guided by pioneer neuroimaging GWAS conducted by Zhao et al[13]. and Elliot
668 et al.[11] We adopted the genome-wide P-value threshold (5×10^{-8}) and annotated independent
669 genetic signals considering linkage disequilibrium (see below). We then estimated the SNP-
670 based heritability using GCTA[37] using the individual-level genotype data with the same
671 covariates in GWAS.

672 To check the robustness of our GWAS results using European ancestry, we performed six
673 sensitivity checks, including *i*) split-sample GWAS by randomly dividing the entire population
674 into two sex and age-matched splits, *ii*) sex-stratified GWAS for males and females, *iii*) non-
675 European GWAS, *iv*) fastGWA[40] for a mixed linear model that accounts for cryptic population
676 stratification, *v*) machine learning-specific GWAS, and *vi*) feature type-specific GWAS.
677
678 **(B): Annotation of genomic loci and genes**: The annotation of genomic loci and mapped genes
679 was performed via FUMA[101] (https://fuma.ctglab.nl/, version: v1.5.0). For the annotation of
680 genomic loci, we first defined lead SNPs (correlation $r^2 \leq 0.1$, distance < 250 kilobases) and
681 assigned them to a genomic locus (non-overlapping); the lead SNP with the lowest P-value (i.e.,
682 the top lead SNP) was used to represent the genomic locus. For gene mappings, three different
683 strategies were considered. First, positional mapping assigns the SNP to its physically nearby
684 genes (a 10 kb window by default). Second, eQTL mapping annotates SNPs to genes based on
685 eQTL associations. Finally, chromatin interaction mapping annotates SNPs to genes when there is
686 a significant chromatin interaction between the disease-associated regions and nearby or distant
687 genes.[101] The definition of top lead SNP, lead SNP, independent significant SNP, and candidate
688 SNP can be found in **Supplementary eMethod 1**.
689
690 **(C): Phenome-wide association query for genomic loci associated with other traits in the**
691 **literature**: We queried the significant independent SNPs within each locus in the GWAS
692 Catalog (query date: January 10th, 2023 via FUMA version: v1.5.0) to determine their
693 previously identified associations with other traits. For these associated traits, we further mapped
694 them into several high-level categories for visualization purposes (**Fig. 2B**).

695

696 **(D): Genetic correlation**: We used LDSC[36] to estimate the pairwise genetic correlation (r_g)
697 between GM, WM, and FC-BAG and several pre-selected traits (**Supplementary eTable 3**) by
698 using the precomputed LD scores from the 1000 Genomes of European ancestry. The following
699 pre-selected traits were included: Alzheimer's disease (AD), autism spectrum disorder (ASD),
700 attention-deficit/hyperactivity disorder (ADHD), obsessive-compulsive disorder (OCD), major
701 depressive disorder (MDD), bipolar disorder (BIP), schizophrenia (SCZ), education and
702 intelligence, as well as the AI-derived subtypes for AD (AD1 and AD2[102]), ASD (ASD1, ASD2,
703 and ASD3[47]), and SCZ (SCZ1 and SCZ2[103]) – serving as more robust endophenotypes than the
704 disease diagnoses themselves. To ensure the suitability of the GWAS summary statistics, we first
705 checked that the selected study's population was European ancestry; we then guaranteed a
706 moderate SNP-based heritability h^2 estimate and excluded the studies with spurious low h^2
707 (<0.05). Notably, LDSC corrects for sample overlap and provides an unbiased estimate of
708 genetic correlation[104]. The h^2 estimate from LDSC is, in general, lower than that of GCTA
709 because LDSC uses GWAS summary statistics and pre-computed LD information and has
710 slightly different model assumptions across different software[105].

711

712 **(E): Partitioned heritability estimate**: Partitioned heritability analysis estimates the percentage
713 of heritability enrichment explained by annotated genome regions[51]. First, the partitioned
714 heritability was calculated for 53 main functional categories. The 53 functional categories are not
715 specific to any cell type, including coding, UTR, promoter, and intronic regions. Details of the
716 53 categories are described elsewhere[51] and are also presented in **Supplementary eTable 5A**.
717 Subsequently, cell type-specific partitioned heritability was estimated using gene sets from

718 Cahoy et al.[58] for three main cell types (i.e., astrocyte, neuron, and oligodendrocyte)
719 (**Supplementary eTable 5B)**.
720
721 **(F): Gene-drug-disease network construction**: We curated data from the Drug Bank database
722 (v.5.1.9)[106] and the Therapeutic Target Database (updated by September 29th, 2021) to construct
723 a gene-drug-disease network. Specifically, we constrained the target to human organisms and
724 included all drugs with active statuses (e.g., patented and approved) but excluded inactive ones
725 (e.g., terminated or discontinued at any phase). To represent the disease, we mapped the
726 identified drugs to the Anatomical Therapeutic Chemical (ATC) classification system for the
727 Drugbank database and the International Classification of Diseases (ICD-11) for the Therapeutic
728 Target Database.
729
730 **(G): Two-sample Mendelian Randomization**: We investigated whether the clinical traits
731 previously associated with our genomic loci (**Fig. 2B**) were a cause or a consequence of GM,
732 WM, and FC-BAG using a bidirectional, two-sample MR approach. GM, WM, and FC-BAG are
733 the outcome/exposure variables in the forward/inverse MR, respectively. We applied five
734 different MR methods using the TwoSampleMR R package[59], including the inverse variance
735 weighted (IVW), MR Egger[107], weighted median[108], simple mode, and weighted mode methods.
736 We reported the results of IVW in the main text and the four others in the **Supplementary eFile**
737 **9**. MR relies on a set of crucial assumptions to ensure the validity of its results. These
738 assumptions include the requirement that the chosen genetic instrument exhibits a strong
739 association with the exposure of interest while remaining free from direct associations with
740 confounding factors that could influence the outcome. Additionally, the genetic variant used in

741 MR should be independently allocated during conception and inheritance, guaranteeing its
742 autonomy from potential confounders. Furthermore, this genetic instrument must affect the
743 outcome solely through the exposure of interest without directly impacting alternative pathways
744 that could influence the outcome (no horizontal pleiotropy). The five MR methods handle
745 pleiotropy and instrument validity assumptions differently, offering various degrees of
746 robustness to violations. For example, MR Egger provides a method to estimate and correct for
747 pleiotropy, making it robust in the presence of horizontal pleiotropy. However, it assumes that
748 directional pleiotropy is the only form of pleiotropy present.

749 To ensure an unbiased selection of exposure variables, we followed a systematic
750 procedure guided by the STROBE-MR Statement[109]. We pre-selected exposure variables across
751 various categories based on our phenome-wide association query. These variables encompassed
752 neurodegenerative diseases (e.g., AD), liver biomarkers (e.g., AST), cardiovascular diseases
753 (e.g., the triglyceride-to-lipid ratio in VLDL), and lifestyle-related risk factors (e.g., BMI).
754 Subsequently, we conducted an automated query for these traits in the IEU GWAS database[110],
755 which provides curated GWAS summary statistics suitable for MR, using the
756 *available_outcomes()* function. We ensured the selected studies used European ancestry
757 populations and shared the same genome build as our GWAS (HG19/GRCh37). Additionally, we
758 manually examined the selected studies to exclude any GWAS summary statistics overlapping
759 with UK Biobank populations to prevent bias stemming from sample overlap[111]. This process
760 yielded a set of seven exposure variables, comprising AD, breast cancer, type 2 diabetes, renin
761 level, triglyceride-to-lipid ratio, aspartate aminotransferase (AST), and BMI. The details of the
762 selected studies for the instrumental variables (IVs) are provided in **Supplementary eTable 6**.

763 We performed several sensitivity analyses. First, a heterogeneity test was performed to
764 check for violating the IV assumptions. Horizontal pleiotropy was estimated to navigate the
765 violation of the IV's exclusivity assumption[64] using a funnel plot, single-SNP MR approaches,
766 and MR Egger estimator[107]. Moreover, the leave-one-out analysis excluded one instrument
767 (SNP) at a time and assessed the sensitivity of the results to individual SNP.
768
769 **(H): PRS prediction**: We calculated the PRS using the GWAS results from the split-sample
770 analyses. The weights of the PRS were defined based on split1 data (training/base data), and the
771 split2 GWAS summary statistics were used as the test/target data. The QC steps for the base data
772 are as follows: *i*) removal of duplicated and ambiguous SNPs for the base data; *ii*) clumping the
773 base GWAS data; *iii*) pruning to remove highly correlated SNPs in the target data; *iv*) removal of
774 high heterozygosity samples in the target data; *v*) removal of duplicated, mismatching and
775 ambiguous SNPs in the target data. After rigorous QC, we employed two methods to derive the
776 three BAG-PRS in the split2 population: *i*) PLINK with the classic C+T method (clumping +
777 thresholding) and *ii*) PRS-CS[57] with a Bayesian approach.
778 To determine the "best-fit" PRS P-value threshold, we performed a linear regression
779 using the PRS calculated at different P-value thresholds (0.001, 0.05, 0.1, 0.2, 0.3, 0.4, 0.5),
780 controlling for age, sex, total intracellular volume, brain position during scanning (lateral,
781 transverse, and longitudinal), and the first forty genetic PCs. A null model was established by
782 including only the abovementioned covariates. The alternative model was then constructed by
783 introducing each BAG-PRS as an extra independent variable.

784 **Data Availability**

785 The GWAS summary statistics corresponding to this study are publicly available on the

786 MEDICINE knowledge portal (https://labs.loni.usc.edu/medicine).

Code Availability

The software and resources used in this study are all publicly available:

- MLNI: https://anbai106.github.io/mlni/, brain age prediction (V0.1.2)
- MEDICINE: https://labs.loni.usc.edu/medicine, knowledge portal for dissemination and GWAS summary statistics sharing
- MUSE: https://www.med.upenn.edu/sbia/muse.html, image preprocessing for GM-IDP
- PLINK: https://www.cog-genomics.org/plink/, GWAS and PRS
- FUMA: https://fuma.ctglab.nl/, gene mapping, genomic locus annotation
- GCTA: https://yanglab.westlake.edu.cn/software/gcta/#Overview, heritability estimates, and fastGWA
- LDSC: https://github.com/bulik/ldsc, genetic correlation, partitioned heritability
- TwoSampleMR: https://mrcieu.github.io/TwoSampleMR/index.html, MR
- PRS-CS: https://github.com/getian107/PRScs, PRS

Competing Interests

None

803 **Authors' contributions**

804 Dr. Wen has full access to all the data in the study and takes responsibility for the integrity of the

805 data and the accuracy of the data analysis.

806 *Study concept and design*: Wen

807 *Acquisition, analysis, or interpretation of data*: Wen

808 *Drafting of the manuscript*: Wen

809 *Critical revision of the manuscript for important intellectual content*: all authors

810 *Statistical analysis*: Wen

References

1. Rajpurkar, P., Chen, E., Banerjee, O. & Topol, E. J. AI in health and medicine. *Nat Med* **28**, 31–38 (2022).
2. Hassabis, D., Kumaran, D., Summerfield, C. & Botvinick, M. Neuroscience-Inspired Artificial Intelligence. *Neuron* **95**, 245–258 (2017).
3. Lee, J. *et al.* Deep learning-based brain age prediction in normal aging and dementia. *Nat Aging* **2**, 412–424 (2022).
4. Wen, J. *et al.* Genetic, clinical underpinnings of subtle early brain change along Alzheimer's dimensions. 2022.09.16.508329 Preprint at https://doi.org/10.1101/2022.09.16.508329 (2022).
5. Hollon, T. *et al.* Artificial-intelligence-based molecular classification of diffuse gliomas using rapid, label-free optical imaging. *Nat Med* 1–5 (2023) doi:10.1038/s41591-023-02252-4.
6. Cole, J. H., Marioni, R. E., Harris, S. E. & Deary, I. J. Brain age and other bodily 'ages': implications for neuropsychiatry. *Mol Psychiatry* **24**, 266–281 (2019).
7. Jones, D. T., Lee, J. & Topol, E. J. Digitising brain age. *The Lancet* **400**, 988 (2022).
8. Tian, Y. E. *et al.* Heterogeneous aging across multiple organ systems and prediction of chronic disease and mortality. *Nat Med* 1–11 (2023) doi:10.1038/s41591-023-02296-6.
9. Kaufmann, T. *et al.* Common brain disorders are associated with heritable patterns of apparent aging of the brain. *Nat Neurosci* **22**, 1617–1623 (2019).
10. Shen, L. & Thompson, P. M. Brain Imaging Genomics: Integrated Analysis and Machine Learning. *Proceedings of the IEEE* **108**, 125–162 (2020).

833 11. Elliott, L. T. *et al.* Genome-wide association studies of brain imaging phenotypes in UK
834 Biobank. *Nature* **562**, 210–216 (2018).
835 12. Smith, S. M. *et al.* An expanded set of genome-wide association studies of brain imaging
836 phenotypes in UK Biobank. *Nat Neurosci* **24**, 737–745 (2021).
837 13. Zhao, B. *et al.* Genome-wide association analysis of 19,629 individuals identifies variants
838 influencing regional brain volumes and refines their genetic co-architecture with cognitive
839 and mental health traits. *Nat Genet* **51**, 1637–1644 (2019).
840 14. Zhao, B. *et al.* Common genetic variation influencing human white matter microstructure.
841 *Science* **372**, (2021).
842 15. Wen, J. *et al.* Novel genomic loci and pathways influence patterns of structural covariance
843 in the human brain. 2022.07.20.22277727 Preprint at
844 https://doi.org/10.1101/2022.07.20.22277727 (2022).
845 16. Grasby, K. L. *et al.* The genetic architecture of the human cerebral cortex. *Science* **367**,
846 eaay6690 (2020).
847 17. Brouwer, R. M. *et al.* Genetic variants associated with longitudinal changes in brain
848 structure across the lifespan. *Nat Neurosci* **25**, 421–432 (2022).
849 18. Zhao, B. *et al.* Common variants contribute to intrinsic human brain functional networks.
850 *Nat Genet* **54**, 508–517 (2022).
851 19. Smith, S. M. *et al.* Brain aging comprises many modes of structural and functional change
852 with distinct genetic and biophysical associations. *eLife* **9**, e52677.
853 20. Ning, K. *et al.* Improving brain age estimates with deep learning leads to identification of
854 novel genetic factors associated with brain aging. *Neurobiology of Aging* **105**, 199–204
855 (2021).

21. Leonardsen, E. H. *et al.* Genetic architecture of brain age and its causal relations with brain and mental disorders. *Mol Psychiatry* 1–10 (2023) doi:10.1038/s41380-023-02087-y.

22. Jonsson, B. A. *et al.* Brain age prediction using deep learning uncovers associated sequence variants. *Nat Commun* **10**, 5409 (2019).

23. Kendler, K. & Neale, M. Endophenotype: a conceptual analysis. *Mol Psychiatry* **15**, 789–797 (2010).

24. Bycroft, C. *et al.* The UK Biobank resource with deep phenotyping and genomic data. *Nature* **562**, 203–209 (2018).

25. Emdin, C. A., Khera, A. V. & Kathiresan, S. Mendelian Randomization. *JAMA* **318**, 1925–1926 (2017).

26. Varoquaux, G. *et al.* Assessing and tuning brain decoders: Cross-validation, caveats, and guidelines. *NeuroImage* **145**, 166–179 (2017).

27. Samper-González, J. *et al.* Reproducible evaluation of classification methods in Alzheimer's disease: Framework and application to MRI and PET data. *NeuroImage* **183**, 504–521 (2018).

28. Pedregosa, F. *et al.* Scikit-learn: Machine Learning in Python. *J. Mach. Learn. Res.* **12**, 2825–2830 (2011).

29. de Lange, A.-M. G. & Cole, J. H. Commentary: Correction procedures in brain-age prediction. *Neuroimage Clin* **26**, 102229 (2020).

30. Peng, H., Gong, W., Beckmann, C. F., Vedaldi, A. & Smith, S. M. Accurate brain age prediction with lightweight deep neural networks. *Medical Image Analysis* **68**, 101871 (2021).

878 31. Leonardsen, E. H. *et al.* Deep neural networks learn general and clinically relevant
879 representations of the ageing brain. *NeuroImage* **256**, 119210 (2022).
880 32. Vidal-Pineiro, D. *et al.* Individual variations in 'brain age' relate to early-life factors more
881 than to longitudinal brain change. *eLife* **10**, e69995 (2021).
882 33. Wood, D. A. *et al.* Accurate brain-age models for routine clinical MRI examinations.
883 *Neuroimage* **249**, 118871 (2022).
884 34. More, S. *et al.* Brain-age prediction: A systematic comparison of machine learning
885 workflows. *NeuroImage* **270**, 119947 (2023).
886 35. Bashyam, V. M. *et al.* MRI signatures of brain age and disease over the lifespan based on a
887 deep brain network and 14 468 individuals worldwide. *Brain* **143**, 2312–2324 (2020).
888 36. Bulik-Sullivan, B. K. *et al.* LD Score regression distinguishes confounding from
889 polygenicity in genome-wide association studies. *Nat Genet* **47**, 291–295 (2015).
890 37. Yang, J., Lee, S. H., Goddard, M. E. & Visscher, P. M. GCTA: A Tool for Genome-wide
891 Complex Trait Analysis. *Am J Hum Genet* **88**, 76–82 (2011).
892 38. Buniello, A. *et al.* The NHGRI-EBI GWAS Catalog of published genome-wide association
893 studies, targeted arrays and summary statistics 2019. *Nucleic Acids Res* **47**, D1005–D1012
894 (2019).
895 39. Cheverud, J. M. A COMPARISON OF GENETIC AND PHENOTYPIC
896 CORRELATIONS. *Evolution* **42**, 958–968 (1988).
897 40. Jiang, L. *et al.* A resource-efficient tool for mixed model association analysis of large-scale
898 data. *Nat Genet* **51**, 1749–1755 (2019).

41. Doshi, J. *et al.* MUSE: MUlti-atlas region Segmentation utilizing Ensembles of registration algorithms and parameters, and locally optimal atlas selection. *Neuroimage* **127**, 186–195 (2016).

42. Davatzikos, C., Genc, A., Xu, D. & Resnick, S. M. Voxel-Based Morphometry Using the RAVENS Maps: Methods and Validation Using Simulated Longitudinal Atrophy. *NeuroImage* **14**, 1361–1369 (2001).

43. Hopkins, A. L. & Groom, C. R. The druggable genome. *Nat Rev Drug Discov* **1**, 727–730 (2002).

44. Antibody-Mediated Targeting of Tau In Vivo Does Not Require Effector Function and Microglial Engagement - PubMed. https://pubmed.ncbi.nlm.nih.gov/27475227/.

45. Wilcock, G. K. *et al.* Potential of Low Dose Leuco-Methylthioninium Bis(Hydromethanesulphonate) (LMTM) Monotherapy for Treatment of Mild Alzheimer's Disease: Cohort Analysis as Modified Primary Outcome in a Phase III Clinical Trial. *J Alzheimers Dis* **61**, 435–457.

46. Wen, J. *et al.* Subtyping brain diseases from imaging data. Preprint at https://doi.org/10.48550/arXiv.2202.10945 (2022).

47. Hwang, G. *et al.* Assessment of Neuroanatomical Endophenotypes of Autism Spectrum Disorder and Association With Characteristics of Individuals With Schizophrenia and the General Population. *JAMA Psychiatry* (2023) doi:10.1001/jamapsychiatry.2023.0409.

48. Chand, G. B. *et al.* Two distinct neuroanatomical subtypes of schizophrenia revealed using machine learning. *Brain* **143**, 1027–1038 (2020).

49. International Obsessive Compulsive Disorder Foundation Genetics Collaborative (IOCDF-GC) and OCD Collaborative Genetics Association Studies (OCGAS). Revealing the

922 complex genetic architecture of obsessive-compulsive disorder using meta-analysis. *Mol*
923 *Psychiatry* **23**, 1181–1188 (2018).
924 50. Rietveld, C. A. *et al.* GWAS of 126,559 individuals identifies genetic variants associated
925 with educational attainment. *Science* **340**, 1467–1471 (2013).
926 51. Finucane, H. K. *et al.* Partitioning heritability by functional annotation using genome-wide
927 association summary statistics. *Nat Genet* **47**, 1228–1235 (2015).
928 52. Hoffman, M. M. *et al.* Integrative annotation of chromatin elements from ENCODE data.
929 *Nucleic Acids Res* **41**, 827–841 (2013).
930 53. Haberle, V. & Stark, A. Eukaryotic core promoters and the functional basis of transcription
931 initiation. *Nat Rev Mol Cell Biol* **19**, 621–637 (2018).
932 54. Trynka, G. *et al.* Chromatin marks identify critical cell types for fine mapping complex trait
933 variants. *Nat Genet* **45**, 124–130 (2013).
934 55. Barski, A. *et al.* High-Resolution Profiling of Histone Methylations in the Human Genome.
935 *Cell* **129**, 823–837 (2007).
936 56. Choi, S. W., Mak, T. S.-H. & O'Reilly, P. F. Tutorial: a guide to performing polygenic risk
937 score analyses. *Nat Protoc* **15**, 2759–2772 (2020).
938 57. Ge, T., Chen, C.-Y., Ni, Y., Feng, Y.-C. A. & Smoller, J. W. Polygenic prediction via
939 Bayesian regression and continuous shrinkage priors. *Nat Commun* **10**, 1776 (2019).
940 58. Cahoy, J. D. *et al.* A Transcriptome Database for Astrocytes, Neurons, and
941 Oligodendrocytes: A New Resource for Understanding Brain Development and Function. *J.*
942 *Neurosci.* **28**, 264–278 (2008).
943 59. Hemani, G. *et al.* The MR-Base platform supports systematic causal inference across the
944 human phenome. *eLife* **7**, e34408 (2018).

945 60. Borges, M. C. *et al.* Circulating Fatty Acids and Risk of Coronary Heart Disease and
946 Stroke: Individual Participant Data Meta-Analysis in Up to 16 126 Participants. *J Am Heart*
947 *Assoc* **9**, e013131 (2020).
948 61. Morris, A. P. *et al.* Large-scale association analysis provides insights into the genetic
949 architecture and pathophysiology of type 2 diabetes. *Nat Genet* **44**, 981–990 (2012).
950 62. K, M. *et al.* Association analysis identifies 65 new breast cancer risk loci. *Nature* **551**,
951 (2017).
952 63. Lambert, J.-C. *et al.* Meta-analysis of 74,046 individuals identifies 11 new susceptibility
953 loci for Alzheimer's disease. *Nat Genet* **45**, 1452–1458 (2013).
954 64. Bowden, J. *et al.* A framework for the investigation of pleiotropy in two-sample summary
955 data Mendelian randomization. *Stat Med* **36**, 1783–1802 (2017).
956 65. Burgess, S. & Thompson, S. G. Interpreting findings from Mendelian randomization using
957 the MR-Egger method. *Eur J Epidemiol* **32**, 377–389 (2017).
958 66. Klarin, D. *et al.* Genetics of blood lipids among ~300,000 multi-ethnic participants of the
959 Million Veteran Program. *Nat Genet* **50**, 1514–1523 (2018).
960 67. Nelson, C. P. *et al.* Association analyses based on false discovery rate implicate new loci
961 for coronary artery disease. *Nat Genet* **49**, 1385–1391 (2017).
962 68. Horie, K. *et al.* CSF tau microtubule-binding region identifies pathological changes in
963 primary tauopathies. *Nat Med* **28**, 2547–2554 (2022).
964 69. Gusev, A. *et al.* Partitioning Heritability of Regulatory and Cell-Type-Specific Variants
965 across 11 Common Diseases. *The American Journal of Human Genetics* **95**, 535–552
966 (2014).

967 70. Stamatoyannopoulos, J. A. What does our genome encode? *Genome Res* **22**, 1602–1611
968 (2012).
969 71. Nordestgaard, B. G. & Varbo, A. Triglycerides and cardiovascular disease. *Lancet* **384**,
970 626–635 (2014).
971 72. Antal, B. *et al.* Type 2 diabetes mellitus accelerates brain aging and cognitive decline:
972 Complementary findings from UK Biobank and meta-analyses. *Elife* **11**, e73138 (2022).
973 73. Wu, A. M. L. *et al.* Aging and CNS Myeloid Cell Depletion Attenuate Breast Cancer Brain
974 Metastasis. *Clinical Cancer Research* **27**, 4422–4434 (2021).
975 74. Gkatzionis, A. & Burgess, S. Contextualizing selection bias in Mendelian randomization:
976 how bad is it likely to be? *International Journal of Epidemiology* **48**, 691–701 (2019).
977 75. Sachdev, P. S., Zhuang, L., Braidy, N. & Wen, W. Is Alzheimer's a disease of the white
978 matter? *Curr Opin Psychiatry* **26**, 244–251 (2013).
979 76. Watanabe, K. *et al.* Genome-wide meta-analysis of insomnia prioritizes genes associated
980 with metabolic and psychiatric pathways. *Nat Genet* **54**, 1125–1132 (2022).
981 77. Cermakova, P. *et al.* Parental education, cognition and functional connectivity of the
982 salience network. *Sci Rep* **13**, 2761 (2023).
983 78. Cao, H., Zhou, H. & Cannon, T. D. Functional connectome-wide associations of
984 schizophrenia polygenic risk. *Mol Psychiatry* **26**, 2553–2561 (2021).
985 79. Yu, M., Sporns, O. & Saykin, A. J. The human connectome in Alzheimer disease —
986 relationship to biomarkers and genetics. *Nat Rev Neurol* **17**, 545–563 (2021).
987 80. Tost, H., Champagne, F. A. & Meyer-Lindenberg, A. Environmental influence in the brain,
988 human welfare and mental health. *Nat Neurosci* **18**, 1421–1431 (2015).

989 81. Petersen, R. C. *et al.* Alzheimer's Disease Neuroimaging Initiative (ADNI): clinical
990 characterization. *Neurology* **74**, 201–209 (2010).
991 82. Casey, B. J. *et al.* The Adolescent Brain Cognitive Development (ABCD) study: Imaging
992 acquisition across 21 sites. *Developmental Cognitive Neuroscience* **32**, 43–54 (2018).
993 83. Di Biase, M. A. *et al.* Mapping human brain charts cross-sectionally and longitudinally.
994 *Proceedings of the National Academy of Sciences* **120**, e2216798120 (2023).
995 84. Wen, J. *et al.* Convolutional neural networks for classification of Alzheimer's disease:
996 Overview and reproducible evaluation. *Medical Image Analysis* **63**, 101694 (2020).
997 85. Smith, S. M. *et al.* Tract-based spatial statistics: voxelwise analysis of multi-subject
998 diffusion data. *Neuroimage* **31**, 1487–1505 (2006).
999 86. Tustison, N. J. *et al.* N4ITK: improved N3 bias correction. *IEEE Trans. Med. Imaging* **29**,
1000 1310–1320 (2010).
1001 87. Zhang, H., Schneider, T., Wheeler-Kingshott, C. A. & Alexander, D. C. NODDI: Practical
1002 in vivo neurite orientation dispersion and density imaging of the human brain. *NeuroImage*
1003 **61**, 1000–1016 (2012).
1004 88. Smith, S. M. *et al.* Advances in functional and structural MR image analysis and
1005 implementation as FSL. *Neuroimage* **23 Suppl 1**, S208-19 (2004).
1006 89. Mori, S., Wakana, S., Nagae-Poetscher, L. & van Zijl, P. *MRI Atlas of Human White*
1007 *Matter*. (Elsevier, 2005).
1008 90. Wakana, S. *et al.* Reproducibility of quantitative tractography methods applied to cerebral
1009 white matter. *NeuroImage* **36**, 630–644 (2007).
1010 91. Alfaro-Almagro, F. *et al.* Image processing and Quality Control for the first 10,000 brain
1011 imaging datasets from UK Biobank. *Neuroimage* **166**, (2018).

1012 92. Miller, K. L. *et al.* Multimodal population brain imaging in the UK Biobank prospective
1013 epidemiological study. *Nature Neuroscience* **19**, 1523–1536 (2016).
1014 93. Beckmann, C. F. & Smith, S. M. Probabilistic independent component analysis for
1015 functional magnetic resonance imaging. *IEEE Transactions on Medical Imaging* **23**, 137–
1016 152 (2004).
1017 94. Inference for the Generalization Error | SpringerLink.
1018 https://link.springer.com/article/10.1023/A:1024068626366.
1019 95. Wen, J. *et al.* Characterizing Heterogeneity in Neuroimaging, Cognition, Clinical
1020 Symptoms, and Genetics Among Patients With Late-Life Depression. *JAMA Psychiatry*
1021 (2022) doi:10.1001/jamapsychiatry.2022.0020.
1022 96. Manichaikul, A. *et al.* Robust relationship inference in genome-wide association studies.
1023 *Bioinformatics* **26**, 2867–2873 (2010).
1024 97. Price, A. L., Zaitlen, N. A., Reich, D. & Patterson, N. New approaches to population
1025 stratification in genome-wide association studies. *Nat Rev Genet* **11**, 459–463 (2010).
1026 98. Abraham, G., Qiu, Y. & Inouye, M. FlashPCA2: principal component analysis of Biobank-
1027 scale genotype datasets. *Bioinformatics* **33**, 2776–2778 (2017).
1028 99. Wen, J. *et al.* The Genetic Architecture of Biological Age in Nine Human Organ Systems.
1029 *medRxiv* 2023.06.08.23291168 (2023) doi:10.1101/2023.06.08.23291168.
1030 100. Purcell, S. *et al.* PLINK: A Tool Set for Whole-Genome Association and Population-Based
1031 Linkage Analyses. *Am J Hum Genet* **81**, 559–575 (2007).
1032 101. Watanabe, K., Taskesen, E., van Bochoven, A. & Posthuma, D. Functional mapping and
1033 annotation of genetic associations with FUMA. *Nat Commun* **8**, 1826 (2017).

1034 102. Wen, J. *et al.* Genetic, clinical underpinnings of subtle early brain change along
1035 Alzheimer's dimensions. 2022.09.16.508329 Preprint at
1036 https://doi.org/10.1101/2022.09.16.508329 (2022).
1037 103. Chand, G. B. *et al.* Two distinct neuroanatomical subtypes of schizophrenia revealed using
1038 machine learning. *Brain* **143**, 1027–1038 (2020).
1039 104. Bulik-Sullivan, B. *et al.* An atlas of genetic correlations across human diseases and traits.
1040 *Nat Genet* **47**, 1236–1241 (2015).
1041 105. Zhang, Y. *et al.* Comparison of methods for estimating genetic correlation between
1042 complex traits using GWAS summary statistics. *Brief Bioinform* **22**, bbaa442 (2021).
1043 106. Wishart, D. S. *et al.* DrugBank 5.0: a major update to the DrugBank database for 2018.
1044 *Nucleic Acids Res* **46**, D1074–D1082 (2018).
1045 107. Bowden, J., Davey Smith, G. & Burgess, S. Mendelian randomization with invalid
1046 instruments: effect estimation and bias detection through Egger regression. *Int J Epidemiol*
1047 **44**, 512–525 (2015).
1048 108. Bowden, J., Davey Smith, G., Haycock, P. C. & Burgess, S. Consistent Estimation in
1049 Mendelian Randomization with Some Invalid Instruments Using a Weighted Median
1050 Estimator. *Genet Epidemiol* **40**, 304–314 (2016).
1051 109. Skrivankova, V. W. *et al.* Strengthening the Reporting of Observational Studies in
1052 Epidemiology Using Mendelian Randomization: The STROBE-MR Statement. *JAMA* **326**,
1053 1614–1621 (2021).
1054 110. Elsworth, B. *et al.* The MRC IEU OpenGWAS data infrastructure. 2020.08.10.244293
1055 Preprint at https://doi.org/10.1101/2020.08.10.244293 (2020).

1056 111. Burgess, S., Davies, N. M. & Thompson, S. G. Bias due to participant overlap in two-
1057 sample Mendelian randomization. *Genet Epidemiol* **40**, 597–608 (2016).
1058
1059

Acknowledgments

We want to express our sincere gratitude to the UK Biobank team for their invaluable contribution to advancing clinical research in our field. The primary funding support for this present study is from the initial funding package provided by Stevens Neuroimaging and Informatics Institute, Keck School of Medicine of USC, University of Southern California for WJ. The iSTAGING consortium is a multi-institutional effort funded by NIA by RF1 AG054409 for DC. This research has been conducted using the UK Biobank Resource under Application Number 35148. We thank Caroline O'Driscoll for her work creating the MEDICINE web portal, which has been instrumental in showcasing and disseminating our scientific findings.